Engineering Notebook: Nanocrystalline Nickel Coated Turbopump

Asa Gangjee - Application Reference Number 688239119

2025-2026

Abstract

This project focuses on the development of a mixed-process manufacturing method for a turbopump by combining polymer additive manufacturing with electroless nickel–phosphorus (ENiP) and nanocrystalline nickel coatings. The goal is to produce low-cost, high-strength, cryogenic-compatible turbomachinery components using accessible materials and equipment. Initial testing has demonstrated the successful creation of an ENiP coating, confirming the capability of the plating process to form a dense and mechanically uniform layer. A complete three-stage turbopump and turbine assembly has been modeled and analyzed in CFturbo, with finite element analysis completed to verify that the structure remains within safe stress limits at design rotational speeds.

At this stage, the project remains ongoing, as it was initiated at the beginning of the current school year. The focus is now on improving the nanocrystalline nickel growth system to achieve consistent fine-grain deposition and greater structural reinforcement, and expanding the proven ENiP process to larger parts. While the design, analysis, and preliminary coating results have been completed, no final conclusions are drawn at this time, as further work is required to optimize the electrochemical parameters and integrate the final coating system into the turbopump assembly.

Document Overview

1 Background

Originally developed during Germany's V-2 rocket program in the 1930s, the turbopump was designed to drive propellants into combustion chambers at the high pressures required for efficient rocket operation [1]. The earliest turbopumps employed a single-stage axial impulse gas turbine powered by steam from the catalytic decomposition of hydrogen peroxide [2]. While these systems were able to pressurize propellants effectively, they were extremely inefficient, bulky, and difficult to manufacture [3].

Over the second half of the 20th century, turbopump technology advanced significantly through programs such as NASA's Saturn V and Space Shuttle. Designs, such as those used on the RL10, evolved into complex, multi-stage systems, incorporating multiple turbine stages to improve energy transfer from the working fluid to the pump shaft [4]. These innovations enabled the large-scale space launches of the Shuttle and the rapid transcontinental travel of turbofan aircraft, both powered by turbopumps at their core.

Today, virtually every aerospace propulsion system, from commercial turbofan engines to advanced liquid rocket engines, relies on turbopumps. They remain the most effective means of achieving extremely high mass flow rates and pressures in compact machinery. Modern manufacturers, from Blue Origin, to SpaceX, to Aerojet Rocketdyne continue to iterate on turbopump designs [5], [6], [7]. However, the high precision, advanced materials, and extreme operating environments make turbopumps the single most expensive component of rocket and jet engines. With single unit prices exceeding 150,000 for units supplying a 60,000 lbf engine, turbopumps are an extraordinary cost barrier for startups and researchers alike [8]. For this reason, many student and research teams rely on pressure-fed designs which are heavily restricted in mass flow rate, chamber pressure, and performance.

Material innovation has played a central role in this trend. Whereas early turbopumps were built from heat-treated carbon steels, today's state-of-the-art systems employ additively manufactured nickel-based superalloys that can withstand cryogenic fluids and high turbine outlet temperatures. These materials provide excellent performance but further increase manufacturing complexity and cost.

Recent advances in mixed-material manufacturing now present an alternative. By combining polymer additive manufacturing with the deposition of nickel nanocrystalline coatings, it may be possible to produce turbopump components with comparable strength, corrosion resistance, and cryogenic compatibility at a fraction of the cost. The price diminishment of an alloy coating instead of a homogenous substrate has the ability to significantly lower manufacturing costs. Moreover, deposition processes that use pulsed current may offer faster build rates compared to traditional milling, casting, or metal 3-D printing.

2 Thesis

Developing a novel mixed-process manufacturing methodology for turbopumps by integrating nickel nanocrystalline deposition with polymer-based additive manufacturing to produce low-cost, high-strength, cryogenic-compatible components, enabling the design of a multi-stage centrifugal turbopump at a cost of $400 per unit and manufacturable in less than 48 hours for use in reusable rocket engines, cryogenic propellant feed systems, and high-efficiency aerospace propulsion.

3 Criteria & Constraints

Constraint	Reasoning
Time	Due to the complexity of this project, time is one of the most significant constraints. Specific milestones must be completed to meet deadlines such as the Science and Engineering Fair of Houston submission.
Cost	This project operates on a limited budget of $3,000, constraining part selection, manufacturing options, and procurement flexibility.
Parts	Only consumer-available components may be purchased, restricting flexibility in impeller and turbine geometry and potentially limiting achievable mass flow rates.
Size	The turbopump must be composed of components that fit within a 256 mm^3 print volume or can be discretized into parts that can be printed within this constraint.
Power	I am limited to standard wall outlets supplying a maximum of 1,800 W for electroplating operations, constraining heating and agitation power availability.

Criterion	Reasoning
Impeller mass flow rate of 2 kg/s	Establishes the performance target necessary for comparison to industry-standard turbopump operation.
Turbine mass flow rate of 0.4 kg/s	The turbine must operate within the available dry nitrogen supply, limited to 400 psia and 0.4 kg/s.
Tensile strength of 450 MPa	Printed and plated materials must reach at least 450 MPa tensile strength to withstand cryogenic pressures during operation.
Durable prototype	The turbopump must withstand multiple testing cycles without structural degradation to validate design repeatability.
Cost target of $400	The final turbopump assembly, excluding testing infrastructure, must cost under $400 to demonstrate the feasibility of a low-cost manufacturing approach.
Ease of Manufacturing	The final turbopump design and fabrication process must be executable within 48 hours to validate the practical manufacturability of the proposed method.

4 Design Decision Literature Review

Before beginning experimentation, I first completed a literature review of pertinent information to this project including a summarization of turbopump design options, and different historical attempts to form nanocrystalline nickel structures on polymer substrates.

4.1 Turbopump Design Types

I first decided to define what a turbopump is, and what its major components are using the Sentinel Mission website [1]. The main components of a turbopump are the following: the impeller, a rotating component that generates the necessary centrifugal force to push fluid; the turbine, the energy source that drives the impeller (primarily electric or combustion driven); the casing, the structural support that contains the impeller and turbine and directs the flow of fluid; and the bearings and seals, which support the rotating parts and

prevent any propellant from leaking within the system.

Furthermore, the three main categories of turbopumps are:

- **Centrifugal**, which use a rotating impeller to generate force and increase the fluid's pressure and flow rate.
- **Axial**, which use a multiplicity of radially stacked rotating blades to push the fluid linearly, increasing velocity and pressure.
- **Mixed-flow**, a combination of centrifugal and axial components that balance pressure and flow rate.

This article was impactful in clarifying the distinct turbopump components required for a complete prototype design and providing insight into their integration. It also illuminated the mechanical and operational differences between centrifugal, axial, and mixed-flow configurations, informing my decision-making process. I concluded that a centrifugal turbopump would most likely suit this project because of its compact length, high pressure rise per stage (beneficial for high combustion chamber pressures), and compatibility with cryogenic liquids. However, the insight from this source will continue to guide comparisons of each type's strengths and weaknesses.

4.2 ENiP Adhesion Research

Although I have preliminarily decided to use extrusion 3D printing to build turbopump prototypes, one area of concern is the 3D-printed filament's limited tensile strength, which could lead to structural failure under cryogenic and high-RPM conditions. To address this, I studied *Influence of Electroless Nickel—DLC (Diamond-like Carbon) Multilayer Coating on the Mechanical Performance of the Heat-Treated AlSi10Mg Alloy Produced by Powder Bed Fusion-Laser Beam* by Edigio et al., which examined electroless nickel–phosphorus (ENiP) plating as a reinforcement method to enhance tensile strength [9]. This paper evaluated ENiP as a load-bearing layer on additively manufactured AlSi10Mg and found that the coating significantly improved tensile strength compared to the uncoated alloy.

I also reviewed *Study on Adhesion Properties and Process Parameters of Electroless Deposited Ni-P Alloy for PEEK and Its Modified Materials* by Gao et al., an experimental study demonstrating that ENiP can achieve strong adhesion to high-performance thermoplastics such as PEEK, provided the surface is properly pretreated [10]. These studies suggest that ENiP is viable for use on plastic-based materials to increase tensile strength and structural stability in the turbopump's polymer components. This research has enabled me to conceptualize realistic designs using ENiP coatings to bridge the mechanical gap between printed polymers and metallic performance requirements.

4.3 Nanocrystalline Nickel Structure Synthesis Research

While ENiP provides improved adhesion and moderate strength enhancement, it alone offers limited mechanical reinforcement for polymer-based substrates and is prone to cracking under stress. Consequently, I began investigating pulsed current electrodeposition as a method for forming nickel nanocrystalline structures, characterized by grain sizes of 2–100 nm [11].

The use of nanocrystalline nickel coatings is not widely studied, although companies such as Integran Technologies employ proprietary processes, such as Nanovate, to achieve superalloy-grade performance [12]. However, these methods rely on expensive hardware, specialized chemicals, and labor-intensive procedures, making them impractical for this project. Given the scarcity of open-access research, I plan to experimentally determine optimal parameters for their setup using publicly available information as a foundation.

Currently, I plan to employ a pulsed current electrodeposition process with a 1 ms pulse followed by a 9 ms off-period, as described in [13]. The bath will contain nickel sulfate hexahydrate, boric acid, acetic acid, and saccharin (as a grain refiner). Sulfur content will be varied to tune hardness and ductility, with current densities ranging from 50 $\mathrm{mA/cm^2}$ to 1000 $\mathrm{mA/cm^2}$ supplied from a DC power source switched by a MOSFET.

4.4 Full Shell Construction Summary

A critical step in ensuring polymer turbopump components can withstand cryogenic operation is the creation of a durable metallic midlayer capable of adhering strongly to the base polymer and serving as a foundation for nanocrystalline nickel growth. I have adopted an electroless nickel–phosphorus (ENiP) process to achieve this goal. Because ENiP does not require external current, it can uniformly coat complex geometries.

The process begins with sensitization and activation baths. During sensitization, the polymer surface is immersed in a stannous chloride solution that adsorbs $\mathrm{Sn^{2+}}$ ions onto the surface after mechanical and chemical roughening. These ions act as reducing agents in the subsequent activation bath, where $\mathrm{Pd^{2+}}$ from palladium chloride is reduced to $\mathrm{Pd^0}$ and immobilized on the surface. The resulting palladium particles act as catalytic nucleation sites for ENiP deposition.

Once activated, the part is immersed in an ENiP bath containing nickel sulfate as the $\mathrm{Ni^{2+}}$ source, sodium hypophosphite as the reducing agent, acetic acid for pH control, and sodium citrate as a complexing agent. Citrate moderates $\mathrm{Ni^{2+}}$ availability and prevents uncontrolled precipitation. The primary reaction governing nickel deposition is:

$$\mathrm{Ni^{2+} + 2H_2PO_2^- + 2H_2O \rightarrow Ni(s) + H_2(g) + 2H_2PO_3^- + 2H^+}$$

A midlayer thickness of 50–100 µm is targeted; thin enough to remain ductile yet thick enough to ensure continuity and strong adhesion. The outer nanocrystalline nickel layer will then be deposited through pulsed current electrodeposi-

tion in a nickel sulfamate bath. Pulsed current alternates between short bursts of high current (on the order of 1 ms) and longer relaxation intervals, promoting fine-grain nucleation while limiting coarsening. This produces crystal sizes in the 2–100 nm range, compared to the micron-scale grains typical of DC plating.

Grain refinement leverages the Hall–Petch relationship, which links yield strength inversely to the square root of grain diameter. This results in coatings that combine high hardness and tensile strength with improved ductility. The ENiP midlayer ensures adhesion and strain distribution across the polymer–metal interface, while the nanocrystalline layer provides strength and wear resistance.

Bath additives further influence coating quality. I plan to use saccharin and L-cysteine as additives. Saccharin functions as a grain refiner and internal stress reliever, inhibiting columnar growth and preventing cracking or delamination at high RPM. L-cysteine, a sulfur-containing amino acid, introduces controlled sulfur levels that promote ductility by interrupting brittle grain boundary phases.

Together, these additives yield a nanocrystalline nickel coating with reduced residual stress, finer grain distribution, and increased toughness.

5 Design Overview

I decided to pursue a three-stage gas turbine design with a centrifugal turbopump, pictured in Figure 1. Using stators to accelerate and redirect high-pressure nitrogen at precise angles. The multi-stage design, while an increase in complexity, drastically improves turbine efficiency and allows for greater shaft power from the same pressure drop and mass flow rate of nitrogen. The combination of ENiP and nanocrystal nickel allows a well adhered metal midlayer which is ductile and able to bow with changes in profile associated with cryogenic temperatures with a hard outer layer that provides significant structural support and high performance for the system. To better understand the design process and the simulation tools available to me through partnerships with CFturbo, Simerics, and Ansys, I decided to conduct practice solutions of geometries with known solution topographies. All practice solutions follow the design workflow as described in Section 6.1.

5.1 Parametric Design Process for Turbopump

1. **Define Parameters:** Establish primary inputs including mass flow rate, pressure drop, target RPM, gas temperature, and working fluid. Record derived quantities such as shaft power, efficiency, and specific speed.

2. **Preliminary Geometry:** Determine principal dimensions, velocity triangles, and meridional contours. Select between shrouded or unshrouded configurations and define hub and shroud profiles.

3. **Blade Design:** Generate mean line geometry, specify β angles, and define blade shape, taper, and count.

4. **Stage Configuration:** Add stator–rotor pairs to achieve the desired pressure ratio and power output. Refine each stage through iterative geometric and flow consistency checks.

5. **Pump Definition:** Input design conditions for the centrifugal pump, including mass flow rate, head, RPM, and fluid properties. Adjust allowable stresses and material parameters to match substrate properties.

6. **Verification and Export:** Inspect velocity triangles, Cordier diagrams, and 3D previews for physical consistency. Apply fillets, confirm manufacturability, and export final geometries as `.STEP` files for downstream CAD and simulation analysis or directly into the Ansys Workbench workflow.

5.2 Practice Solution

Figure 1: Version 1 gas turbine and turbopump full design view.

Figure 2: Version 1 gas turbine and turbopump cross section view.

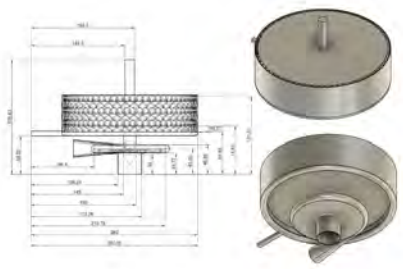

Figure 3: Version 1 gas turbine and turbopump design sketch.

I realized that the turbine should be modeled using the "rocket engine" option for the blades, and so redesigned the turbine with that modification for Version 1. Also, I utilized the video tutorials produced by CFturbo to design the centrifugal impeller.

5.3 Version 1

I have completed a first working draft of the three-stage gas turbine. This draft adheres to the design parameters described in Table 1 for the gas turbine, and 2 for the turbopump. Both the gas turbine and the impeller were designed using CFturbo.

Parameter	**Value**	**Units**
Working fluid	Nitrogen (N_2)	–
Gas constant R	296.8	J/(kg·K)
Ratio of specific heats γ	1.40	–
Total inlet temperature $T_{t,in}$	25	°C
Total inlet pressure $P_{t,in}$	400	psi
Static back pressure P_{out}	14.7	psi
Total pressure ratio $P_{t,in}/P_{t,out}$	27	–
Mass flow rate $\dot{m}_g$	0.40	kg/s
Target shaft speed N	30000	rpm
Required shaft power P_{shaft}	77.94	kW
Number of stages	3	–
Inlet swirl (degrees of reaction)	0.5	deg

Table 1: Gas turbine inputs for design.

Parameter	Value	Units
Pump type	Radial	–
Working fluid	Liquid Nitrogen (LN_2)	–
Density ρ (operating, ≈ 77 K)	804	kg/m^3
Dynamic viscosity μ	1.6×10^{-4}	Pa·s
Vapor pressure P_v (at $\sim$77 K)	14.7	psi
Mass flow rate $\dot{m}_p$	2.00	kg/s
Volume flow rate $Q = \dot{m}/\rho$	2.488×10^{-3}	m^3/s
Target shaft speed N	30000	rpm
Impeller outer diameter limit D_2	150	mm
Specific speed N_s	1.3	–
height		

Table 2: Centrifugal turbopump inputs for design.

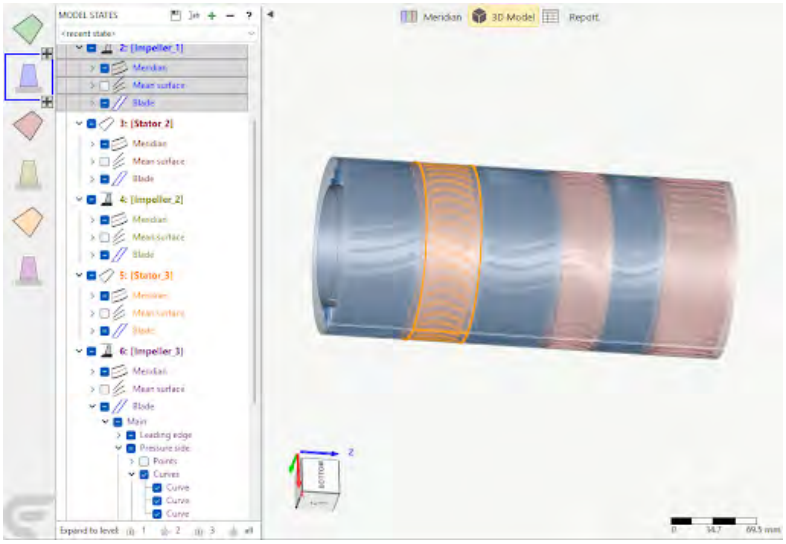

Figure 4: 3-Stage gas turbine 3D view in CFturbo.

Each stage follows a stator–rotor configuration (a total of three stators and three rotors), with the mean blade lines, inlet and outlet angles, and geometric dimensions of each component fully defined to ensure consistent flow turning and pressure rise across stages.

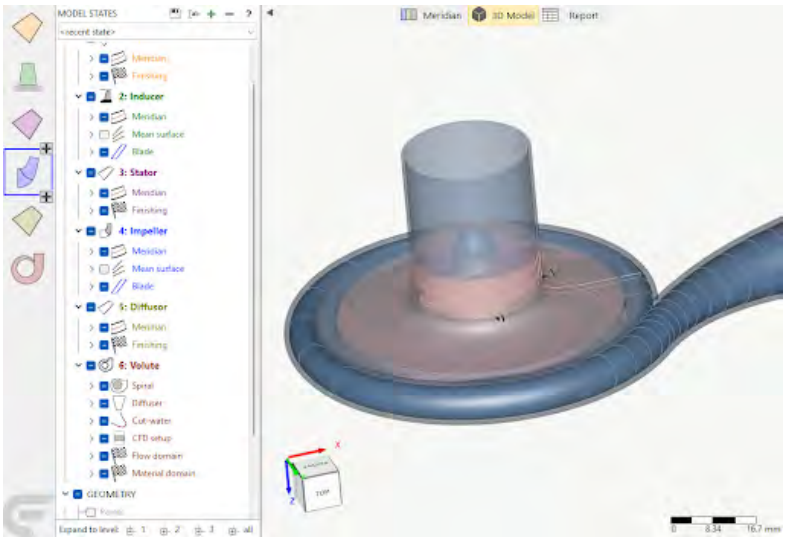

Figure 6: Centrifugal impeller 3D view in CFturbo.

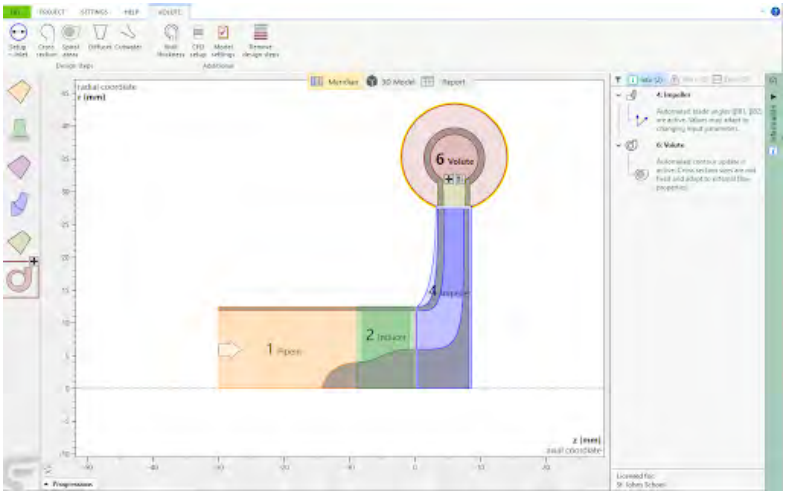

Figure 5: 2-D Sketch contour of turbopump stages for Version 2 in CFturbo.

In addition, I have finalized a second design of the centrifugal impeller.

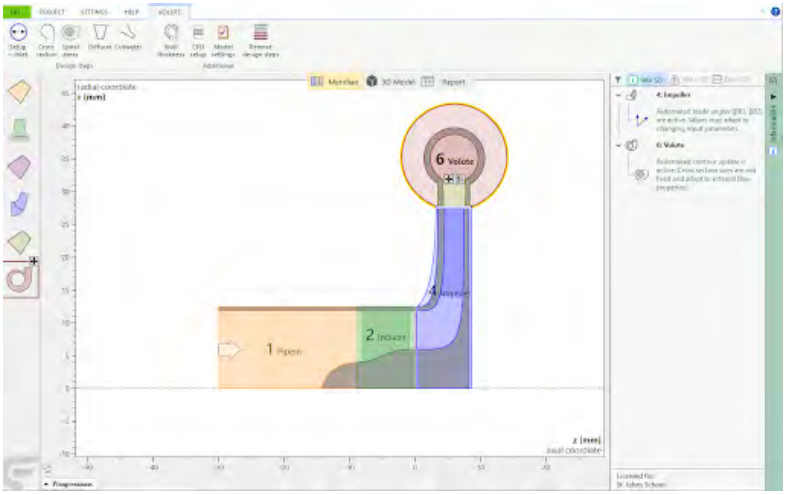

Figure 7: Meridional view of the impeller assembly. The second axial stator is visible as a thin pink line between the inducer and impeller.

The complete impeller assembly consists of:

- **Initial axial stator**, which directs and straightens the incoming flow.
- **Inducer**, which gradually increases the fluid pressure and imparts swirl to help the fluid enter the main impeller smoothly.
- **Second axial stator**, a compact stage that reorients the flow to reduce swirl losses.
- **Centrifugal impeller**, which provides the primary energy transfer by accelerating the fluid radially outward.
- **Diffuser**, which converts the high-velocity fluid into static pressure.
- **Volute**, which collects the fluid and channels it toward the outlet.

5.4 Finite Element Analysis

I conducted rotodynamic stress analysis on the centrifugal impeller and all gas turbine stages. The simulation assumed a rotational velocity of 3,141.592653 rad/s, as that is the design parameter used in CFturbo. A high fidelity, tetrahedral mesh with an average body size of 0.001m was used. The body was constrained around a frictionless supporting center axis and it was assumed that the center of the parts does not warp significantly and allows for a convergent and correct solution.

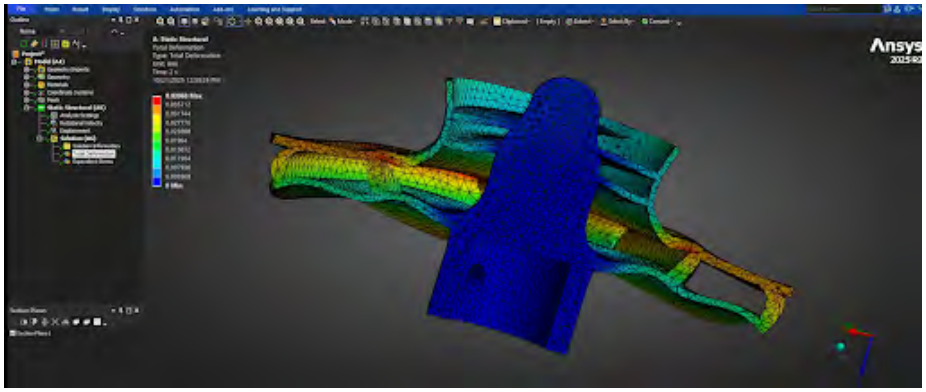

Figure 8: FEA of centrifugal turbopump with deformation displayed (exaggerated scale).

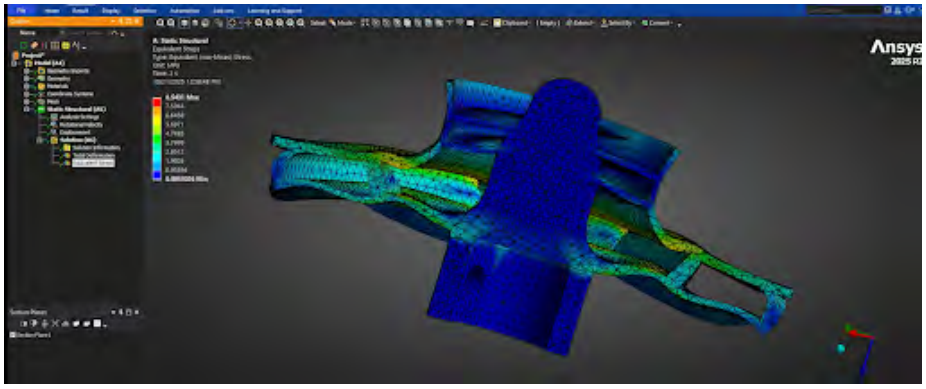

Figure 9: FEA of centrifugal turbopump with equivalent stress displayed (exaggerated scale).

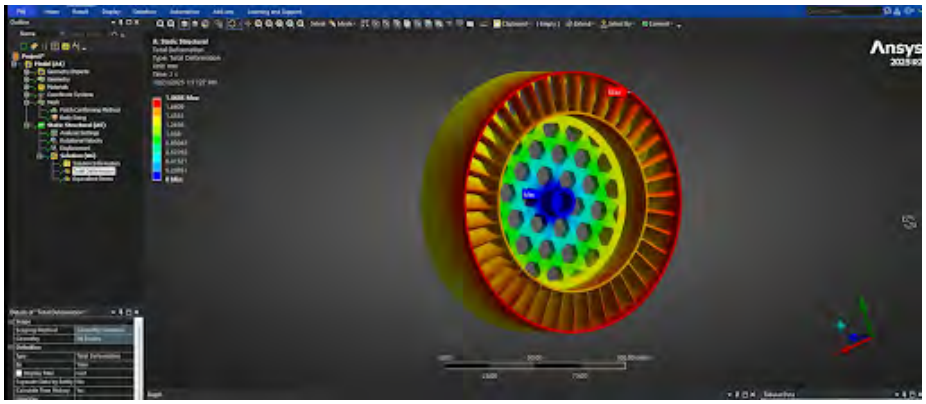

Figure 10: FEA of gas turbine stage 2 with deformation displayed.

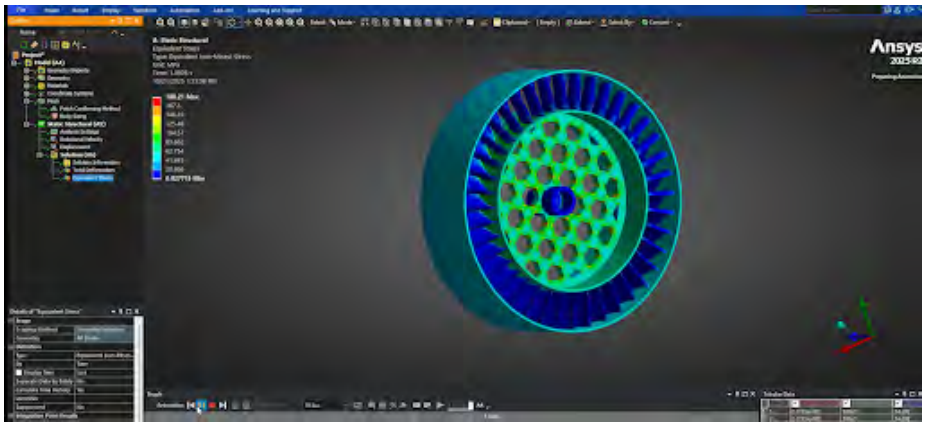

Figure 11: FEA of gas turbine stage 2 with equivalent stress displayed.

5.5 Simulation Results Summary

The finite element analysis predicted maximum equivalent stresses of 8.54 MPa within the impeller hub and 188 MPa within the turbine rotor at the design speed of 3,142 rads/sec. The impeller stress remained below the effective tensile limit of polycarbonate (55.3 MPa), confirming that the component geometry is mechanically feasible. However, the loads on the gas turbine far exceed the limits of polycarbonate. The FEA analysis indicates a load of 188 MPa on the outer edge of a turbine which is solely printed in polycarbonate and of 403 MPa with a turbine which has a predicted density of 3 g/cm^3. Although this is a major simplification as it assumes mass homogeneity and a very thick layer, a homogeneous density approximation does give an effective upper bound of the stresses the turbine might experience. This simulation data essentially provides the minimum safe ultimate tensile strength for the design to function as intended and is the reason for the criteria definition. I will use these simulations to inform design decisions of the turbine hub and attachment mechanism to make sure that design choices fall within a reasonable range for the materials used. I can also use FEA simulations to build tolerances in the design to account for impeller and gas stage warping at high rotational velocities. I plan to do more accurate shell-layer analysis once the nanocrystalline coating material's properties are evaluated.

5.6 ENiP Coating Process Workflow

1. **Surface Preparation:** Roughen 3D printed parts with 1000-grit sandpaper, then rinse in isopropyl alcohol (IPA) and deionized (DI) water. Etch briefly in 0.1 M HCl, rinse, dry, and expose to cold plasma for 5 minutes to increase surface energy.

2. **Sensitization and Activation:** Immerse parts in a stannous chloride

(2–10 g/L) sensitization bath for 2–5 minutes, followed by a palladium chloride (0.04–1 g/L) activation bath for 2–5 minutes to create Pd^0 nucleation sites. Rinse in DI H_2O and dry gently.

3. **ENiP Deposition:** Prepare a bath of 25–30 g/L $NiSO_4 \cdot 6H_2O$, 20–30 g/L $NaH_2PO_2 \cdot H_2O$, 10–15 g/L $Na_3C_6H_5O_7 \cdot 2H_2O$, and 5–10 mL/L CH_3COOH in 500 mL DI H_2O. Heat to 80–92°C with moderate stirring and maintain pH 4.5–5.0 using ammonium hydroxide. Immerse activated parts for 30–60 minutes, observing color change as nickel deposits. If instability occurs, dilute with DI H_2O to stabilize.

4. **Bath Control:** Monitor temperature and pH continuously. Use sodium citrate for buffering and adjust stirring to ensure uniform deposition without disrupting the surface layer.

5. **Post-Treatment:** Rinse coated parts in DI H_2O, neutralize waste with baking soda, and dry in air or a low-temperature oven. Inspect coating uniformity and adhesion before proceeding to subsequent plating or nanocrystalline deposition.

5.7 Pulsed DC Nanocrystalline Nickel Growth Process Workflow

1. **Substrate Preparation:** Verify a uniform ENiP midlayer, rinse in deionized (DI) water, dry with compressed air, and inspect for uniformity. Mask non-conductive regions using electroplating tape.

2. **Electrolyte Preparation:** Dissolve 300–400 g/L nickel sulfamate, 30–40 g/L boric acid, 0.5–2 g/L saccharin, and 0.1–0.5 g/L L-cysteine in DI H_2O. Adjust pH to 3.5–4.5 with ammonium hydroxide or sulfamic acid, then heat to 50–60°C with moderate stirring.

3. **Electrodeposition Setup:** Arrange a pure nickel anode parallel to the cathodic substrate at 50–70 mm spacing. Connect to a programmable pulsed DC power supply capable of millisecond switching, ensuring complete immersion and good electrical contact.

4. **Pulse Parameters:** Set $t_{on} = 1$ ms, $t_{off} = 9$ ms, peak current density 50–1000 mA/cm^2, and a 10% duty cycle. Confirm waveform accuracy on an oscilloscope and use solid-state switching for precise control.

5. **Deposition:** Plate for 30–90 minutes to achieve 5–20 µm coatings. Maintain temperature and pH stability, agitate gently to prevent gradients, and observe surface color for uniform growth. Continuous DC operation must be avoided to preserve nanocrystalline grain structure.

6. **Post-Treatment:** Rinse parts in DI H_2O, dry below 60°C, and optionally anneal at 200–250°C for 1 hour to relieve internal stress. Inspect coatings microscopically for uniformity and adhesion.

7. **Safety and Disposal:** Neutralize waste with sodium carbonate or baking soda, collect nickel-containing residues separately, and clean all glassware with DI H_2O before storage in labeled containers.

6 Coating Trials Overview

One of the most significant aspects of this project is the chemistry needed to produce a well-adhering ENiP and nanocrystalline layer to the substrate. I decided to first research which materials might be well suited to high performance applications at low temperature. The materials seclected for testing are PVDF, Nylon-12, and Polycarbonate.

6.1 ENiP Solution 1: Initial Trial

The first ENiP bath appeared light green and darkened gradually as heat was applied. Nickel began depositing on the sample surfaces near 60 °C. As the temperature reached 80 °C, a light nickel haze formed on the glass walls of the beaker. Although mild wall deposition is occasionally observed in ENiP systems, the extent of hazing suggested possible contamination on the glass surface.

At 85 °C, the film thickened and began detaching from the walls due to convection currents, indicating a mass nickel precipitation event and an unstable bath. Two main causes were considered:

1. An excessively acidic solution, which can drive premature nickel reduction.

2. Overheating beyond the thermal stability of the bath.

Temperature measurements using a secondary thermal probe confirmed that the bath did not exceed the 90 °C upper limit, ruling out thermal degradation. pH testing showed an acidic range between 3 and 4, well below the required 4.5–5.0 range. I concluded that the bath synthesis procedure was incomplete and lacked a step to raise pH.

Ammonium hydroxide was selected as the corrective base, since it does not form insoluble nickel precipitates or cause unwanted side reactions. As the solution cooled, noticeable gas evolution occurred from the nickel clumps, likely hydrogen produced by the reduction reaction:

$$Ni^{2+} + 2H_2PO_2^- + 2H_2O \longrightarrow Ni(s) + H_2(g) + 2H_2PO_3^- + 2H^+$$

After cooling and cessation of gas evolution, sodium bicarbonate was added to neutralize the remaining acid. The neutralized residue was evaporated and safely disposed of. Future trials will incorporate controlled addition of ammonium hydroxide to achieve and maintain pH 4.5–5.0, monitored with a calibrated pH probe during heating.

6.2 ENiP Solution 2: pH Stabilization Attempt

To minimize potential material loss from another bath crash, a smaller-volume ENiP solution was prepared. Tensile testing blanks were degreased with isopropyl alcohol, mechanically roughened, chemically etched in 0.1 M HCl, rinsed in DI H_2O, and plasma-treated prior to sensitization and activation.

The sensitization and activation baths were reused from the first trial. Plasma treatment appeared only mildly effective after 48 hours, suggesting that future treatments should be conducted immediately prior to plating. The bath pH measured 4.68 at the start of deposition. Upon immersion of the blanks, vigorous bubbling occurred and the pH abruptly dropped to 3.93, signaling a bath crash.

I reduced bath temperature and slowly added ammonium hydroxide dropwise until pH stabilized at 4.63. Gas evolution decreased significantly as the bath equilibrated. Over a 35-minute treatment, acetic acid and 6 M ammonium hydroxide were alternately added to maintain pH between 4.5 and 5.0.

The pH instability indicated insufficient buffering capacity, prompting the conclusion that future baths should include additional sodium citrate. After 35 minutes, bubbling ceased completely, suggesting depletion of nickel ions. In future tests, fewer blanks will be coated simultaneously or larger baths will be used to prevent rapid exhaustion. Treatment duration will also be extended to one hour to ensure complete and uniform coating, as several blanks from this trial exhibited patchy, weakly adhered nickel layers.

This trial provided quantitative evidence of the causes of bath instability and established effective methods for pH stabilization.

6.3 ENiP Solution 3: Stabilization via Proprietary Additive

Figure 12: Samples from ENiP solution 3 displayed. From left to right the sample materials are polycarbonate, PVDF, nylon, polycarbonate, and nylon.

A third ENiP bath was prepared on October 8, 2025, using 5.71 g glacial acetic acid, 27.00 g nickel sulfate hexahydrate, 22.08 g sodium hypophosphite monohydrate, and 13.63 g sodium citrate. The clear green solution behaved similarly to prior formulations. However, as temperature approached 60 °C, light hazing developed on the glass walls, and at 80–85 °C, rapid nickel precipitation again occurred.

To prevent material loss, I added a small amount of Caswell's commercial *OnePlate* ENiP solution to the bath [14]. The addition immediately halted the precipitation and stabilized the solution. Based on patent literature, the stabilizing effect is likely due to trace lead or similar compounds that inhibit uncontrolled nickel reduction and aggregation.

I concluded that while the base ENiP chemistry was correct, the absence of a stabilizing component caused repeated bath crashes. Subsequent trials will use the same core formulation, supplemented with a small quantity of Caswell's *OnePlate* concentrate to moderate the redox kinetics and maintain ionic stability throughout deposition.

Solution 3 resulted in the plating of 2 nylon samples, 2 polycarbonate samples, and 1 PVDF sample, shown in Figure 12. The PVDF sample displayed very poor adhesion to the nickel as the nickel was easy to rub off by hand, and, as such, was not continued with for further testing. The polycarbonate also

had somewhat poor surface adhesion, but displayed a significant improvement in tensile strength in early testing, so was pursued for later baths. The nylon samples had by far the best surface adhesion, but they seemingly decreased in ultimate tensile strength. For this reason, I decided that further data was needed, so both nylon and polycarbonate were pursued for ENiP 4.

6.4 ENiP Solution 4: Hybrid Formulation and Material Evaluation

Figure 13: Experimental ENiP plating setup showing suspended polymer test strips.

Figure 14: ENiP-coated polymer samples following deposition. The uniform metallic luster indicates continuous nickel coverage and successful stabilization of the plating bath during the fourth formulation trial.

In the fourth iteration, I combined the established ENiP formulation with the Caswell's *OnePlate* concentrate, which had previously demonstrated stabilizing behavior. The bath composition included:

- 5.16 g nickel sulfate hexahydrate
- 4.07 g sodium hypophosphite monohydrate
- 1.00 g sodium citrate
- glacial acetic acid to adjust pH

The commercial concentrate was mixed at a 7.5:1 ratio (DI H_2O to concentrate), as recommended by the manufacturer. The final pH was adjusted to 3.5–4.5 using acetic acid, consistent with the product safety documentation.

Plating performance was stable and consistent across all nine test samples (4 polycarbonate samples and 5 nylon samples). The resulting nickel coatings were uniform, dense, and lustrous with an average thickness of $25\mu m$. Minor pinholing was observed but was not significant. Electrical testing indicated a resistance of approximately 1.8 Ω, confirming a continuous, conductive metallic layer suitable for nanocrystalline electrodeposition.

Tensile tests showed failure at 31.65 MPa, significantly below the substrate's original strength, suggesting that prolonged exposure to the acidic bath weakened the base nylon material. This is supported by literature, as nylon is not

compatible with acetic acid, which was overlooked in the foundational literature review [15]. I, therefore, plan to transition to polycarbonate substrates for subsequent trials to improve mechanical performance.

7 Material Strength Testing Data for ENiP Coated Parts

Table 3: Nylon with ENiP coating (25.00 µm). Stress computed as $\sigma = F/A$ with F in N and A in mm^2.

ID	Area (mm^2)	Break Force (N)	Stress (MPa)
NE1	1.63	51.00	31.38
NE2	1.63	55.00	33.85
NE3	6.25	195.00	31.20
NE4	6.25	199.00	31.84
NE5	6.25	201.00	32.16
NE6	6.25	192.00	30.72
NE7	6.25	190.00	30.40
	Mean $\pm$ *SD*: 31.65 ± 1.14 MPa		($n = 7$)

Table 4: Nylon with no coating.

ID	Area (mm^2)	Break Force (N)	Stress (MPa)
NB1	4.00	168.00	42.00
NB2	4.00	160.00	40.00
NB3	4.00	162.00	40.50
NB4	4.00	165.00	41.25
NB5	4.00	167.00	41.75
	Mean $\pm$ *SD*: 41.10 ± 0.84 MPa		($n = 5$)

Table 5: Polycarbonate with ENiP coating (25.00 µm).

ID	Area (mm^2)	Break Force (N)	Stress (MPa)
PE1	1.63	107.00	65.85
PE2	1.63	105.00	64.62
PE3	6.25	400.00	64.00
PE4	6.25	407.00	65.12
PE5	6.25	383.00	61.28
PE6	6.25	399.00	63.84
	Mean $\pm$ *SD*: 64.12 ± 1.57 MPa		$(n = 6)$

Table 6: Polycarbonate with no coating.

ID	Area (mm^2)	Break Force (N)	Stress (MPa)
PB1	0.90	64.00	71.11
PB2	2.25	76.00	33.78
PB3	2.00	127.00	63.50
PB4	2.10	124.00	59.05
PB5	1.54	70.00	45.45
PB6	3.80	234.00	61.58
PB7	1.43	80.00	55.94
	Mean $\pm$ *SD*: 55.77 ± 12.45 MPa		$(n = 7)$

Table 7: Summary of group statistics and coating effect. Δ is coated minus bare mean stress for the same polymer.

Material	Bare Mean (MPa)	Coated Mean (MPa)	Δ (MPa)
Nylon	41.10	31.65	−9.45
Polycarbonate	55.77	64.12	8.34

7.1 Material Behavior

The data collected during tensile tests is critical for moving forward with designing the turbopump. All tested samples of the nylon fractured brittlely, which is non ideal behavior for components which will be subject to cryogenic exposure. Also, the significant decrease in ultimate tensile strength of the nylon coupons indicates that the acidic bath had adverse effect on the material properties of the samples. For this reason in particular, I decided to only move forward with coupons made of polycarbonate.

7.2 Nanocrystalline Bath Trial 1: Overly Acidic Bath

Following the successful stabilization of the ENiP process and verification of mechanical improvement in coated substrates, attention shifted to the development of the nanocrystalline nickel layer intended to serve as the final structural coating. This stage aimed to achieve sub-100 nm grain sizes and a yield strength approaching that of commercial superalloys while maintaining the adhesion of the ENiP foundation.

The first nanocrystalline nickel plating trial failed to produce crystalline growth. The 0.5 L bath was composed of:

- 159.37 g nickel sulfamate (318.74 g/L)
- 13.59 g boric acid (27.18 g/L)
- 1.93 g saccharin (3.86 g/L)
- 0.06 g L-cysteine (0.12 g/L)

I identified two likely causes for failure:

1. **Temperature too low:** The bath was maintained at 40 °C instead of the required 60–65 °C, increasing solution resistance and limiting current density below the threshold needed for nucleation.
2. **Improper pH adjustment:** Ammonium hydroxide was used to raise the pH, but its addition caused rapid opacity and inhibited deposition. Future experiments will avoid ammonium hydroxide and instead rely on citrate buffering to maintain stable pH.

Future nanocrystalline trials will employ proper thermal control and revised pH stabilization to ensure consistent nucleation and fine-grain growth.

8 System Integration

To combine the previously modeled and simulated gas turbine and centrifugal turbopump, I used Fusion360 to CAD the complete system. The two main systems are attached to a piece of metal bar stock, pictured in Figure 15, which improves structural rigidity and allows the full system to easily be mounted

to a larger body. The design utilizes shrouded bearings for their resistance to extremely high rotation speeds, and a 3/8" D-shaft to mount the full system to. The current design utilizes a single turbopump, but I would like to move to a two pump design after a singular pump design is experimentally verified, as the turbopump now could account for both fuel and oxidizer delivery to the engine.

Figure 15: Cut through of full Version 1 system.

The turbine will be driven by a high pressure nitrogen supply from a regulator and tank unlike a standard open or closed cycle expander turbopump system. I chose this design, as it significantly lowers system complexity. The full system with the nitrogen supply is rendered in Figure 16.

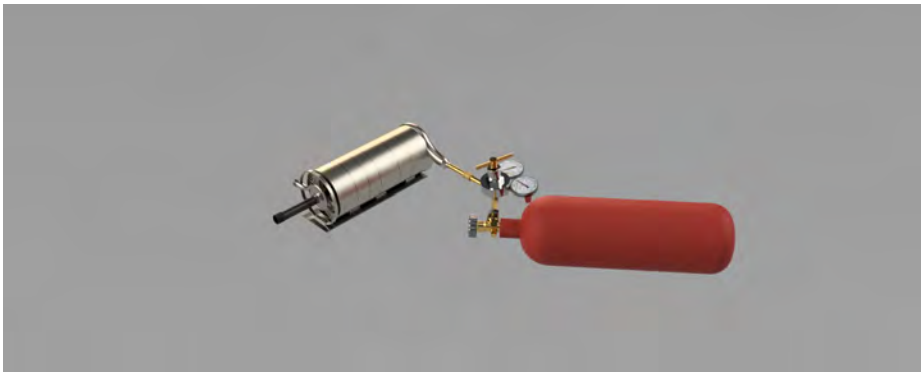

Figure 16: Render of full turbopump system Version 1 design with nitrogen tank and regulator.

9 Next Steps

1. **Material Transition:** Replace nylon substrates with polycarbonate to eliminate acid-induced degradation during ENiP deposition and to improve coating adhesion. Get more data with this final material combination.

2. **Nanocrystalline Nickel Optimization:** Continue refinement of the pulsed DC plating parameters to promote columnar grain growth and minimize intergranular phosphorus segregation. Future experiments will adjust duty cycle, current density, and bath pH to achieve a consistent grain size below 50 nm across the full substrate surface.

3. **Surface Characterization:** Perform scanning electron microscopy (SEM) and nanoindentation testing on coated samples to validate grain morphology of noncrystalline structure.

4. **Thermal and Mechanical Validation:** Conduct non-homogeneous, high-temperature FEA using the measured coating properties to simulate performance under turbine operational loads. Compare results against the baseline uncoated polymer rotor to quantify the effective increase in allowable wall stress and fatigue life.

5. **Prototype Assembly:** Integrate coated components into the full turbopump housing for non-cryogenic drive testing. Record pressure rise, flow rate, and bearing stability during operation to confirm mechanical viability.

6. **Cryogenic Adaptation:** Begin the design of a cryogenic test rig capable of operating with LN_2 to evaluate coating performance and structural stability under thermal shock and low-temperature contraction.

7. **System Compatibility:** Combine turbopump with aerospike rocket engine which has also been plated with ENiP and nanocrystal layers. Collect data from full system hot fires to confirm the validity of nanocrystalline technology in full system aerospace applications.

References

[1] tinelmis, "Turbopump - Definition Detailed Explanation - Rocketry Propulsion Glossary - Sentinel Mission," 07 2025.

[2] Stokes, P. R., "Hydrogen Peroxide for Power & Propulsion," *Proceedings (historical/technical paper)*, 1998, See p. 9: V-2 feed by a centrifugal system with a single-stage impulse turbine driven by decomposed peroxide.

[3] Sobin, A. J. and Bissell, W. R., "Turbopump Systems for Liquid Rocket Engines," Tech. Rep. NASA SP-8107, NASA Lewis Research Center, 1974, Table of turbine-drive cycle tradeoffs: monopropellant GG has low performance and high weight; peroxide turbine boost systems described as complex (separate catalyst/generator).

[4] "Turbopump systems for liquid rocket engines," *ntrs.nasa.gov*, 08 1974.

[5] Joyce, C. M., Tyebjee, S. T., Klimov, I. V., and Rizzolo, Z. D., "Self-optimizing seal for turbomachinery, and associated systems and methods," 2024, Describes a variable-balance-ratio face seal for turbopumps in rocket engines.

[6] NASA Spinoff, "Space Program Pumps Up Turbomachinery," 2023, Describes Merlin turbopumps built by Barber-Nichols and heritage from NASA FASTRAC.

[7] "RL10 Propulsion System Specification," Tech. rep., L3Harris (Aerojet Rocketdyne), 2024.

[8] Council, N. R., "Rocket Propulsion Systems for Access to Space," *A Review of United States Air Force and Department of Defense Aerospace Propulsion Needs*, The National Academies Press, Washington, DC, 2006, pp. 148–150, Fastrac/MC-1 turbomachinery unit cost targets and TPA requirements.

[9] Egidio, G. D., Martini, C., Ceschini, L., and Morri, A., "Influence of Electroless Nickel—DLC (Diamond-like Carbon) Multilayer Coating on the Mechanical Performance of the Heat-Treated AlSi10Mg Alloy Produced by Powder Bed Fusion-Laser Beam," *Materials*, Vol. 16, 04 2023, pp. 3313–3313.

[10] Gao, S., Wu, C., Yang, X., Cheng, J., and Kang, R., "Study on Adhesion Properties and Process Parameters of Electroless Deposited Ni-P Alloy for PEEK and Its Modified Materials," *Coatings*, Vol. 13, No. 2, 2023.

[11] Yuan, R., Beyerlein, I. J., and Zhou, C., "Emergence of grain-size effects in nanocrystalline metals from statistical activation of discrete dislocation sources," *Acta Materialia*, Vol. 90, 2015, pp. 169–181.

[12] Tomantschger, K., Nagarajan, N., Kowpak, T., Gonzalez, F., Neacsu, M., Brooks, I., Wang, A., and Ronis, T., "Nanometal-Polymer Hybrids: Application of High Strength Nanocrystalline Metallic Structural Layers on Thermoplastic Articles," *Jahrbuch Oberflaechentechnik*, Vol. 67, 01 2011.

[13] Tritjahjono, R. I., "Synthesis of nanocrystalline nickel via pulsed current electrodeposition in additive-free deposition bath and comparison of nanoscale characterization," *Eastern-European Journal of Enterprise Technologies*, Vol. 1, 02 2024, pp. 13–19.

[14] "Caswell One-Plate® 1 Electroless Nickel Solution," 2025.

[15] "Nylon Chemical Compatibility Chart," 2025.